Atmos. Chem. Phys. Discuss., 15, 19045–19077, 2015
www.atmos-chem-phys-discuss.net/15/19045/2015/
doi:10.5194/acpd-15-19045-2015

Atmospheric Chemistry and Physics Discussions

Spectral optical layer properties of cirrus from collocated airborne measurements – a feasibility study

F. Finger[1], F. Werner[1,2], M. Klingebiel[3], A. Ehrlich[1], E. Jäkel[1], M. Voigt[3], S. Borrmann[3,4], P. Spichtinger[3], and M. Wendisch[1]

[1]Leipzig Institute for Meteorology (LIM), University of Leipzig, Leipzig, Germany
[2]University of Maryland (UMBC), Physics Department, Baltimore, Maryland, USA
[3]Institute for Atmospheric Physics, Johannes Gutenberg University Mainz, Mainz, Germany
[4]Max Planck Institute for Chemistry, Mainz, Germany

Received: 24 April 2015 – Accepted: 7 June 2015 – Published: 10 July 2015

Correspondence to: F. Finger (f.finger@uni-leipzig.de)

Published by Copernicus Publications on behalf of the European Geosciences Union.

Abstract

Spectral optical layer properties of cirrus are derived from simultaneous and vertically collocated measurements of spectral upward and downward solar irradiance above and below the cloud layer and concurrent in situ microphysical sampling. From the irradiance data spectral transmissivity, absorptivity, reflectivity, and cloud top albedo of the observed cirrus layer are obtained. At the same time microphysical properties of the cirrus were sampled. The close collocation of the radiative and microphysical measurements, above, beneath and inside the cirrus, is obtained by using a research aircraft (Learjet 35A) in tandem with a towed platform called AIRTOSS (AIRcraft TOwed Sensor Shuttle). AIRTOSS can be released from and retracted back to the research aircraft by means of a cable up to a distance of 4 km. Data were collected in two field campaigns above the North and Baltic Sea in spring and late summer 2013. Exemplary results from one measuring flight are discussed also to illustrate the benefits of collocated sampling.

Based on the measured cirrus microphysical properties, radiative transfer simulations were applied to quantify the impact of cloud particle properties such as crystal shape, effective radius r_{eff}, and optical thickness τ on cirrus optical layer properties. The effects of clouds beneath the cirrus are evaluated in addition. They cause differences in the layer properties of the cirrus by a factor of 2 to 3, and for cirrus radiative forcing by up to a factor of 4. If low-level clouds below cirrus are not considered the solar cooling due to the cirrus is significantly overestimated.

1 Introduction

Significant uncertainties in atmospheric modelling and remote sensing originate from clouds and their effects and interaction with solar and terrestrial radiation (IPCC, 2013). In particular, cirrus clouds are critical; they can either warm or cool the atmosphere, depending on cloud optical properties and altitude (Lynch et al., 2002). Cirrus clouds glob-

ACPD
15, 19045–19077, 2015

ally occur at all latitudes and in all seasons with a mean global cover of about 20–30 %. More than 70 % of cirrus are observed in the tropics (Wylie et al., 1994), being relatively stable and long-lived (Liou, 1986). Due to different meteorological conditions and evolution processes cirrus clouds are characterized by a wide diversity of macrophysical structure, size and number of ice particles, crystal shape and orientation. Horizontal and vertical inhomogeneities of these properties increase the complexity of cirrus. The radiative layer properties (reflectivity, transmissivity, and absorptivity) of cirrus depend on the microphysical (effective radius r_{eff}, ice water content) and optical (absorption, scattering) characteristics.

Cirrus inhomogeneities impact (i) the energy budget of the Earth's atmosphere, and (ii) the remote sensing of cirrus optical thickness τ and r_{eff} which is mostly based on one-dimensional (1-D) radiative transfer modelling. Schlimme et al. (2005) found that the horizontal variability of the extinction coefficient leads to significant differences in the solar irradiance compared to a homogeneous cloud, resulting in a varying transmittance of about 80 %. Zhang et al. (1999) reported that the radiative forcing of the cirrus may switch sign depending on the geometry and size of the ice crystals. The impact of ice crystal shape on the cirrus radiative forcing, depending on the solar zenith angle, can vary between 10 and 26 % for the solar spectral range (Wendisch et al., 2005), while for the thermal infrared even differences of up to 70 % are found (Wendisch et al., 2007). Eichler et al. (2009) investigated the influence of ice crystal shape on the retrieval of τ and r_{eff} and reported effects of up to 70 % (τ) and 20 % (r_{eff}).

Measurements of spectral layer properties of cirrus are rare. Commonly a combination of measurements and simulations is applied to derive layer properties, whereby τ and r_{eff} are retrieved from reflected radiance (airborne or spaceborne, see Francis et al., 1998) and then used in combination with a radiative transfer model to simulate layer reflectivity, transmissivity, and absorptivity.

Direct measurements of cirrus optical layer properties are hard to obtain if only one aircraft is used. Usually, the radiative measurements above and below the cirrus are performed consecutively (e.g., Pilewskie and Valero, 1992). This method unavoidably

ACPD
15, 19045–19077, 2015

involves a temporal shift between the two measurements above and below the cloud and, thus, can be applied for rather static and horizontal homogeneous cloud layers only. Therefore, e.g., helicopter-borne towed platforms have been developed and adapted, such as the Airborne Cloud Turbulence Observation System (ACTOS) for microphysical in situ instruments, and the Spectral Modular Airborne Radiation measurement syTem – HELIOS (SMART–HELIOS) for solar spectral reflectivity measurements (Henrich et al., 2010; Werner et al., 2013, 2014). For cirrus measurements, Frey et al. (2009) introduced the aircraft-borne AIRTOSS (AIRcraft TOwed Sensor Shuttle), shown in Fig. 1. In this paper we present an extended version of AIRTOSS with additional spectral radiation sensors.

In Sect. 2 the instrumentation of the aircraft and AIRTOSS is described. In particular the collocated radiation instruments and their combination to derive optical layer properties are discussed in Sect. 3. In Sect. 4 the calculated layer properties and the concurrent microphysical observations are introduced for one exemplary measurement case. Based on these measurements radiative transfer simulations are performed and analyzed in Sect. 5.

2 Instrumentation

The instruments were mounted at different positions on the aircraft, the towed platform AIRTOSS, and an additional wing pod underneath the left wing as illustrated in Fig. 2a. The operation of the Learjet 35A together with the tethered AIRTOSS is certified for altitudes up to 12.5 km (the previous limitation was 7.6 km; Frey et al., 2009).

2.1 Aircraft

The applied aircraft certified for the operation of AIRTOSS is a Learjet 35A, operated by GFD (Gesellschaft für Flugzieldarstellung) GmbH. Instruments for measurements of trace gases and water vapor are mounted inside the cabin with special inlets sampling

ACPD
15, 19045–19077, 2015

ambient air from outside the aircraft during the flight. An upward looking radiation sensor, measuring the downward irradiance $F^{\downarrow}$ (in $W\,m^{-2}\,nm^{-1}$), was mounted on the fuselage including the Spectral Modular Airborne Radiation measurement syTem (SMART) inside the aircraft, introduced by Wendisch et al. (2001), further developed by Bierwirth et al. (2009). Optical fibers connect the optical inlet with two Zeiss Spectrometers for the visible to near infrared (300–2200 nm) wavelength range with a resolution of 2–3 nm (visible) and 9–16 nm (near infrared), respectively. An active horizontal stabilization platform (Wendisch et al., 2001) was operated to keep the horizontal positioning of the upward looking optical inlet on the top of the aircraft during the aircraft measurements. A pod mounted under the left wing of the aircraft contains another optical inlet with a set of spectrometer, measuring the upward irradiance. A Forward Scattering Spectrometer Probe (FSSP–100), placed at the tip of the wing pod, measures the cloud particle number size distribution (size diameter range from 2 to 47 µm, Gayet et al., 2002). To correct for shattering (Korolev et al., 2013) the FSSP–100 records the particle-by-particle data (Field et al., 2003, 2006). The instrument was mainly used as indicator for the time periods when the aircraft was inside clouds and for coarse estimates of general parameters like mean cloud particle diameter.

2.2 AIRTOSS

AIRTOSS, as shown in Fig. 2b, has a length of 2.85 m and a diameter of 24 cm; the maximum payload is 40 kg. It can be released from and retracted to the aircraft by a 4 km long towing cable.

In the front part the Cloud Combination Probe (CCP, see e.g., Wendisch and Brenguier, 2013; Klingebiel et al., 2015) is installed. The CCP consists of the Cloud Droplet Probe (CDP) and the Cloud Imaging Probe instrument (CIP grey scale – denoted as CIPgs in the following). The CDP method is similar to the FSSP–100 and detects particles in the size diameter range between 2 and 50 µm by measuring the forward-scattered light of individual particles. The CIPgs records two-dimensional (2-D) shadow images of the particles and covers a size range between 15 and 960 µm with an opti-

ACPD
15, 19045–19077, 2015

cal resolution of 15 µm. The performance of these microphysical cloud probes in cirrus clouds was characterized by McFarquhar et al. (2007).

The center part of AIRTOSS contains the battery for power supply, sufficient to cover a time period of about two hours. The radiation setup is mounted in the backward part of AIRTOSS. It consists of two spectrometer pairs and two optical inlets, one upward and one downward looking, measuring the spectral irradiance F. Additional sensors for temperature and relative humidity, latitude, longitude and position angles pitch, roll and heading of AIRTOSS are installed.

The housing of the towed platform consists of an aerodynamic canister to avoid irregular movements and to enable quiet flying, being crucial for reliable radiation measurements (Frey et al., 2009).

3 Optical layer properties

Four optical inlets, two for upward and two for downward irradiance were mounted on the Learjet 35A and AIRTOSS. This setup enables to simultaneously measure the irradiance in two different altitudes (e.g., above and below cloud) as required to calculate cloud layer properties (see Fig. 3). By measuring the upward and downward irradiance above (top) and below (base) a cloud layer the optical properties are derived as follows. The reflectivity R is given by:

$$R = \frac{F^{\uparrow}_{\text{top}} - F^{\uparrow}_{\text{base}}}{F^{\downarrow}_{\text{top}}}. \quad (1)$$

R quantifies the relative portion of incoming solar radiation that is reflected by the cloud layer. The transmissivity T of a cloud layer is defined by:

$$T = \frac{F^{\downarrow}_{\text{base}}}{F^{\downarrow}_{\text{top}}}. \quad (2)$$

ACPD
15, 19045–19077, 2015

It describes the part of the incoming irradiance transmitted through the cloud. The relative portion of irradiance absorbed inside the cloud layer is defined by the absorptivity:

$$A = \frac{\left(F^{\downarrow}_{\text{top}} - F^{\uparrow}_{\text{top}}\right) - \left(F^{\downarrow}_{\text{base}} - F^{\uparrow}_{\text{base}}\right)}{F^{\downarrow}_{\text{top}}}. \quad (3)$$

From these definitions it follows:

$$R + T + A = \frac{F^{\uparrow}_{\text{top}} - F^{\uparrow}_{\text{base}} + F^{\downarrow}_{\text{base}} + F^{\downarrow}_{\text{top}} - F^{\uparrow}_{\text{top}} - F^{\downarrow}_{\text{base}} + F^{\uparrow}_{\text{base}}}{F^{\downarrow}_{\text{top}}} = 1. \quad (4)$$

The cloud top albedo R_{top} is given by:

$$R_{\text{top}} = \frac{F^{\uparrow}_{\text{top}}}{F^{\downarrow}_{\text{top}}}. \quad (5)$$

R_{top} describes the cloud reflection property of the cloud layers and the underlying surface. For investigating the effect of the cirrus layer on the atmospheric radiative energy budget the radiative forcing (RF_{toa}) at the top of atmosphere (toa) is used, defined by:

$$\text{RF}_{\text{toa}} = \left(F^{\downarrow}_{\text{toa}} - F^{\uparrow}_{\text{toa}}\right)_{\text{cloud}} - \left(F^{\downarrow}_{\text{toa}} - F^{\uparrow}_{\text{toa}}\right)_{\text{clear sky}}. \quad (6)$$

The subscripts “cloud” and “clear sky” indicate measurements/simulations in a clear sky atmosphere and under cloudy conditions. A positive RF_{toa} indicates a warming effect of the cloud on the atmosphere, whereas a negative RF_{toa} stands for a cooling effect.

ACPD
15, 19045–19077, 2015

4 Observations

Measurements were performed during two AIRTOSS – ICE observational campaigns in spring (6–8 May) and late summer (29 August–5 September) in 2013. The research flights were based at the military airports in Hohn and Jagel, North Germany, and were carried out in restricted areas above the North and Baltic Sea. The measurement areas represent boxes with the size of 50 km × 80 km, and 35 km × 80 km, respectively. Stepwise horizontal flight legs were performed to collect radiative and microphysical data in different altitudes (6–11.5 km). The transport of tropospheric air masses into the stratosphere was reported by Mueller et al. (2015). In total twelve measurement flights were carried out during both campaigns; four of them were analyzed in detail.

Here we present measurements of the flight eastern of the German island of Rügen above the Baltic Sea (54.15–54.9° N, 13.9–14.3° E), performed on 4 September 2013 (08:53–10:17 UTC). Northern Germany was under the influence of a warm front with associated cirrus and the center of the low above Denmark (see Fig. 4). Figure 4a shows the corresponding composite satellite image of METEOSAT–10. In the image the high cirrus clouds are illustrated by white colors. Low clouds are indicated by yellow colors and were present over a large area, including parts of the measurement area. The flight track of the Learjet 35A inside this area is shown in Fig. 4b.

4.1 Microphysical measurements

Figure 5 shows the vertical profiles of (a) static air temperature (in °C), (b) relative humidity (in %) with respect to ice, measured by instruments on the aircraft, and of (c) number concentration (in cm^{-3}) and (d) mean diameter (in µm), measured by the CCP on AIRTOSS. The bars quantify the measurement errors, resulting from instrument uncertainties (a, b), counting statistics (c), and determination of the depth of field (d). The horizontal dashed line indicates the altitude above which stratospheric air was encountered (Mueller et al., 2015). Considering the measured ice particle number concentra-

ACPD
15, 19045–19077, 2015

tion the cirrus was identified in altitudes between 8.6 and 10.3 km and in a temperature range of −32 to −46 °C.

Figure 5c and d show the particle number concentration and mean diameter as a function of altitude. Each data point is a mean value for a 200 m height interval. With increasing altitude the mean particle diameter decreases while the number concentration increases. Due to sedimentation and related aggregation processes the larger cloud particles can be found in the lower cloud parts. A more precise depiction of the mean particle diameter shows Fig. 6a with the associated number size distributions for selected flight paths at certain altitudes in (b). The distribution maximum is shifted from lower to higher diameters with increasing height and ranges from 30 to 300 µm.

4.2 Radiation data

4.2.1 Spectral irradiances

In Fig. 7a the time series of downward and upward irradiance measured by AIRTOSS at a wavelength of 550 nm is illustrated for the entire flight: gray for downward and light blue for upward irradiance. The altitude (red line in Fig. 7b) shows the stepwise flight pattern and the different altitudes of the level legs. The gray shaded area indicates the vertical extent of the cirrus. The gray colored peaks in the time series of the irradiance (Fig. 7a) are due to flight manoeuver and have to be excluded from further analysis. The measured pitch and roll angles of the AIRTOSS were used to sort out the data assuming a threshold of 5°. Resulting are the thickened line periods marking the measuring points at straight flight legs. The almost constant values of the downward irradiance (0.95–1.05 $W\,m^{-2}\,nm^{-1}$) are a result of the thin cirrus layer above the sensor. The upward irradiance is influenced by the surface albedo and changing conditions due to underlying clouds; they show values between 0.5 and 0.9 $W\,m^{-2}\,nm^{-1}$ at 550 nm.

As the AIRTOSS is dragged behind the aircraft time allocation of the radiation measurements of the towed platform have to be adjusted to those measured simultaneously on the Learjet 35A to guarantee vertical collocation. The temporal shift between Learjet

ACPD
15, 19045–19077, 2015

and AIRTOSS was calculated by using the cable length (914 m), aircraft velocity (150–170 m s^{-1}) and altitude difference of both platforms, that is dependent of the velocity. The resulting altitude and time difference varies between 160 and 210 m, corresponding to 4.8 to 6 s.

Measured spectra of upward and downward irradiance from both platforms are shown in Fig. 8 at the two times I and II, indicated by the dashed lines in Fig. 7. The two spectra represent different conditions below the cirrus: in case II a cloud is below the cirrus, in case I the atmosphere below the cirrus is cloudless. The vertical difference between the two measurement platforms is 185 m during the time period I–II. The downward irradiance $F^{\downarrow}_{\text{top}}$ at the top of the cloud layer was simulated (Mayer and Kylling, 2005). The black solid lines show the irradiance, measured in the flight altitude of the Learjet above the cloud layer (subscript top), the black dotted lines represent the irradiance measured from the AIRTOSS from below the cirrus (subscript base). As expected, the downward irradiance below the cirrus ($F^{\downarrow}_{\text{base}}$) is significantly lower than measured above ($F^{\downarrow}_{\text{top}}$) for both cases I and II. This shows that the attenuation of the solar radiation (reflection and absorption by cirrus particles) by the observed cirrus is significant. Upward irradiance ($F^{\uparrow}_{\text{top}}$ and $F^{\uparrow}_{\text{base}}$) at time II is relatively high. This is due to the low clouds which were present below the cirrus at time II. In case of a clear atmosphere between cirrus and ocean surface (time I), lower upward irradiance was measured. Due to the high altitude, about 10.5 km, no water vapor absorption bands are revealed in the near infrared spectra as shown by the almost unaffected downward irradiance in both levels. Therefore, all absorption measured in the downward irradiance below the cirrus originates from the cirrus only.

The upward radiation depends on the albedo of the Earth's surface and underlying clouds, visible in higher values of upward irradiance, especially in (b). The absorption bands of liquid water at wavelengths of 1140 or 1400 nm are obvious from the spectra.

ACPD
15, 19045–19077, 2015

4.2.2 Spectra of reflectivity, absorptivity, transmissivity

By measuring the spectral upward and downward irradiance collocated at two different altitudes the cloud optical layer properties of the cloud layer in between according the Eqs. (1)–(3) are derived.

Figure 8c and d show the spectral transmissivity (red, see Eq. 2), reflectivity (black, see Eq. 1), absorptivity (green, see Eq. 3), and cloud top albedo (gray, see Eq. 5) in the visible and near infrared wavelength range according to the examples in Fig. 8a and b. The error bars result from the Gaussian error propagation due to uncertainties of calibration, cosine correction, dark current, and signal to noise ratio. The resulting percentage errors range between 5.0 and 6.0 % with higher values for the near infrared wavelength range.

As cirrus clouds are optically thin, the transmissivity dominates over the entire spectral range with high values between 60 and almost 100 % in both cases. The reflectivity in Fig. 8c (no low-level cloud) is not higher than about 12 % and in Fig. 8d (with low-level cloud) 15 % due to a brighter water cloud underneath. The same effect is indicated by the cloud top albedo showing higher values of about 30 % for case II in the depicted wavelength range.

The transmissivity shows a negative spectral slope, absorptivity a positive trend, and the reflectivity shows no spectral trend. As the imaginary part of the refractive index is associated with the absorption coefficient which increases with increasing wavelength, the measured absorptivity in (c) and (d) shows a spectral trend with a positive slope and values up to 40 % in the near infrared range, pointing out the importance of cirrus clouds in this wavelength range. Furthermore, case II with the brighter lower cloud leads to a lower absorptivity in the wavelength range of 1000 to 1500 nm because of horizontal photon transport in the cloud layer.

A time series of the cloud optical layer properties (at 1640 nm) is given in Fig. 9, with (a) transmissivity, (b) absorptivity, and (c) reflectivity, for the cirrus layer between 10.6 and 10.8 km altitude and a distance of 25.9 km. The cloud top albedo from below the

ACPD
15, 19045–19077, 2015

aircraft (black triangles), representing the cirrus and low-level cloud, and from below AIRTOSS (gray spheres), representing only the low-level cloud, is plotted in (d).

The layer properties show small variations due to a thin cirrus layer. The transmissivity shows the smallest variation between 0.768 and 0.796. Absorptivity and reflectivity range between 0.103 and 0.142, and 0.078–0.111, resulting in a percentage difference of 38 and 29 %, respectively, but still within the error bars. The two trends of R_{top} show the effect of changing properties of the underground on the cloud top albedo. As the cirrus layer is thin, R_{top} from above the cirrus is also affected by the surface albedo and bright underlying water clouds with a varying R_{top} of about 25 % and significant differences in the absolute values. The difference between both is due to the absorption of the cirrus layer in between the two measurement altitudes.

5 Radiative transfer simulation

5.1 Model introduction

To compare the measurements with simulations and to quantify the impact of different parameters such as cloud particle shape and size on cirrus cloud optical layer properties, sensitivity studies with the one-dimensional (1-D) radiative transfer model libRadtran (Mayer and Kylling, 2005) including the DISORT (DIScrete ORdinate Radiative Transfer) code by Stamnes et al. (2000) are performed. The observed cirrus layer is represented by varying cloud properties and the corresponding upward and downward irradiance at the top and the base of the cirrus are calculated to obtain the optical layer properties reflectivity, absorptivity, and transmissivity (according to Eqs. 1–3), and the cloud top albedo and radiative forcing (Eqs. 5–6). The needed volumetric extinction coefficient $\langle b_{\mathrm{ext},\lambda}\rangle$, single-scattering albedo $\langle \omega_\lambda\rangle$, and phase function $\langle p_\lambda\rangle$ are derived by combining calculated tables of single scattering properties by Yang et al. (2005) with in situ measured number size distributions $\mathrm{d}N/\mathrm{d}D$ (in cm^{-3}) from the CCP (see Sect. 4.1) installed on AIRTOSS. The single scattering properties for individual parti-

ACPD
15, 19045–19077, 2015

cles (extinction coefficient $C_{\mathrm{ext},\lambda}$, scattering coefficient $C_{\mathrm{sca},\lambda}$, single-scattering albedo ω_λ, and phase function p_λ) with different particle radii are weighted with the number size distribution. The spectral volumetric extinction coefficient $\langle b_{\mathrm{ext},\lambda}\rangle$ in units of km^{-1} was obtained by (see Wendisch et al., 2005):

$$\langle b_{\mathrm{ext},\lambda}\rangle = \int C_{\mathrm{ext},\lambda} \cdot \frac{\mathrm{d}N}{\mathrm{d}D} \cdot \mathrm{d}D. \tag{7}$$

The bound of integration is defined by the size diameter range of the CCP. A similar algorithm was used to derive the spectral volumetric single-scattering albedo $\langle \omega_\lambda\rangle$ by calculating:

$$\langle \omega_\lambda\rangle = \frac{\int \omega_\lambda \cdot C_{\mathrm{ext},\lambda} \cdot \frac{\mathrm{d}N}{\mathrm{d}D} \cdot \mathrm{d}D}{\langle b_{\mathrm{ext},\lambda}\rangle}. \tag{8}$$

Furthermore, the volumetric phase function $\langle p_\lambda\rangle$ is obtained by:

$$\langle p_\lambda\rangle = \frac{\int p \cdot C_{\mathrm{sca},\lambda} \cdot \frac{\mathrm{d}N}{\mathrm{d}D} \cdot \mathrm{d}D}{\int C_{\mathrm{sca},\lambda} \cdot \frac{\mathrm{d}N}{\mathrm{d}D} \cdot \mathrm{d}D}. \tag{9}$$

5.2 Simulated and measured spectra for a single cirrus layer

To investigate the effect of different ice crystal shapes (see Fig. 10), a fixed number size distribution is combined with different shape assumptions: Solid Column, Column 8 Elements, Plate, Plate 10 Elements, Hollow Bullet Rosette, Droxtal, and a mixture of 30 % Plates (10 Elements), 30 % Hollow Bullet Rosettes, 20 % Plates, and 20 % Hollow Columns, similar to the mixture described by Baum et al. (2005). The multi-component ice crystals are aggregates consisting of their respective number of crystals. The different crystal shapes are introduced by Yang et al. (2013). The ice crystal roughness is set to smooth, see Baum et al. (2010).

ACPD
15, 19045–19077, 2015

Included in the simulations is a measured number size distribution (see (1) in upper panel of Fig. 11), where the microphysical data is obtained by in situ measurements from a 100 s part of the flight on 4 September 2013 with a mean diameter of about 18 µm. The simulated cirrus layer is located between 8.6 and 10.3 km altitude.

Figure 10 shows the measured (diamonds) and simulated (lines) spectral optical layer properties transmissivity T (a), reflectivity R (b), and absorptivity A (c) for those seven crystal shapes. Additionally, the cloud top albedo R_{top} (d) and the simulated radiative forcing RF_{toa} (see Eq. 6) in (e) are represented. As reference case the shape Droxtal (red line) is used approximating spherical particles. The measurement example is case I from Fig. 7 without a low-level cloud below the cirrus.

The results show, that varying ice crystal shape causes differences that are spectrally dependent, especially for absorptivity in the near infrared wavelength range between 1450 and 1800, and 1900 and 2200 nm, where the imaginary part of the refractive index of ice shows a maximum. This corresponds to an increased absorption coefficient and, therefore, a more pronounced shape effect in this wavelength range. A similar spectral trend of the shape effect shows the transmissivity.

The percentage difference of transmissivity between the varying shapes and the reference case ranges between 5 and 50 %. The lowest differences show Solid Columns and Hollow Bullet Rosettes, whereas the mixture according to Baum et al. (2005) and Plates (10 Elements) show highest values. The shape variability is more pronounced for reflectivity and absorptivity with differences of up to 70 and 100 % for Plates (10 Elements), respectively. The cloud top albedo shows a similar behaviour such as the reflectivity, but with highest differences of up to 70 % for Plates (10 Elements) inside the wavelength range of water vapor absorption.

In relation to the highest values of reflectivity the corresponding radiative forcing for Solid Columns and Droxtals are lowest with −0.21 and $-0.18\,W\,m^{-2}\,nm^{-1}$ (at 550 nm) and for Plates (10 Elements) and the mixture according to Baum et al. (2005) highest with −0.05 and $-0.06\,W\,m^{-2}\,nm^{-1}$ (550 nm), respectively, resulting in more pronounced

ACPD
15, 19045–19077, 2015

cooling effects for Droxtals and Solid Columns. This leads to a difference in the radiative forcing of up to a factor of 4 assuming different shapes.

Additionally, the gray diamonds represent the measurement case I (see Fig. 8c). Discrepancies between the measured and simulated curves result from the variety of cloud properties. Especially the cloud top albedo shows a large difference due to the influence of the surface albedo and the atmospheric layer underneath the high cirrus.

The calculations, presented in Fig. 11a–e, include varying number size distributions from different 100 s parts (1)–(6), shown in the upper panel, from in situ measurements from the flight of 4 September 2013. For comparison the particular size distribution included in the calculations for Fig. 10 is shown here assuming a mixture of particle shapes according to Baum et al. (2005) (red line).

The variabilities are smaller than for varying crystal shapes, but with a similar spectral trend showing pronounced effects for T and A in the near infrared range excluding the ranges of the water vapor absorption bands. As the number size distribution defines the optical thickness of the cloud influencing the optical layer properties, the resulting optical thicknesses are between 0.03 and 0.61 for effective radii r_{eff} between 16 and 44 µm. This results in the highest transmissivity and lowest reflectivity for the case with the lowest optical thickness causing differences of up to 17 and 95 %, respectively, to the reference case with $\tau = 0.61$. The absorptivity varies in the range of the ice particle absorption and causes a difference of up to 95 % between the optically thinnest and thickest clouds, whereas the cloud top albedo shows a similar difference of up to 95 % in the wavelength range of water vapor absorption.

According to the changes in the layer properties the radiative forcing varies most between those cases while the absolute differences are small, varying between −0.005 and $-0.06\,\mathrm{W\,m^{-2}\,nm^{-1}}$ (at 550 nm).

5.3 Cirrus and underlying low-level cloud

Because frequently low clouds were observed during the flights the effect of a low-level water cloud was investigated, too. Figure 12 shows two cirrus cases, one with (black

ACPD
15, 19045–19077, 2015

line) and one without (red line) a low-level water cloud. The cirrus is the same reference case as in Fig. 11. For the second case a water cloud ($\tau = 45$) was added between 1.5 and 1.75 km altitude. The measurement example is the same shown in Fig. 8d (case II from Fig. 7).

Adding a low-level cloud in the simulation leads to a higher transmissivity (up to 7 %) and lower reflectivity (up to 180 %) of the cirrus layer except in the wavelength ranges of the water vapor absorption bands. As the cloud top albedo is no cirrus layer property it shows the largest difference for the low-level cloud case, but a good agreement with the measurement case in the shortwave-infrared wavelength range.

For characterizing the effect of the cirrus on the atmosphere's energy budget when an additional low water cloud is present a modified radiative forcing RF'_{Ci}

$$RF'_{Ci} = RF_{Ci+low\ cloud} - RF_{low\ cloud} \tag{10}$$

$$RF'_{Ci} = F^{\uparrow}_{low\ cloud} - F^{\uparrow}_{Ci+low\ cloud}$$

is introduced. The resulting RF'_{Ci} is the difference between the case of a cirrus with underlying low water cloud and the case with the low cloud only (as Keil and Haywood, 2003 applied for aerosol layers) at top of atmosphere.

RF'_{Ci} is shown in Fig. 11e (black line) in contrast to the radiative forcing RF (see Eq. 6) of the same but undisturbed cirrus (red line). It is noticeable that there is a sign changing effect on RF' with negative values for the visible spectral range and a positive radiative forcing in the near infrared range. This leads to an overestimation of the cooling effect of the cirrus with a percentage difference of about 80 % in the visible wavelength range and up to a factor of 4 in the near infrared range.

6 Conclusions

Spectra of optical layer properties of cirrus have been derived from collocated airborne radiation measurements in the framework of the AIRTOSS – ICE (AIRcraft TOwed Sensor Shuttle – Inhomogeneous Cirrus Experiment) project. Two field campaigns have

ACPD
15, 19045–19077, 2015

taken place above the North and Baltic Sea in spring and late summer 2013. Collocated measurements by an aircraft (Learjet 35A) and the towed platform AIRTOSS, released on a towing cable underneath the plane, are collected above, beneath and inside the cirrus. For radiation measurements the straight flight legs with minor changes of pitch and roll movements of the measurement platform are used.

Spectral upward and downward irradiance in the visible and near infrared wavelength range above and below the cirrus have been measured to derive the spectral transmissivity, absorptivity, reflectivity, and cloud top albedo of the observed cirrus layer. Irradiance spectra and a time series for a straight flight leg of 4 September 2013 are analyzed. The resulting layer properties at one wavelength in the near infrared (1640 nm) differ due to horizontal inhomogeneities and the influence of low-level clouds, but with an increased effect due to low clouds in the cloud top albedo with varying values of up to 25 %.

The impact of varying ice crystal shape and cloud particle size distribution is studied with a 1-D RTM in combination with volumetric extinction coefficient, single-scattering albedo, and phase function calculated from measured in situ size distributions and tables of ice crystal single-scattering properties. The results show the highest sensitivity in cloud optical layer properties for varying ice crystal shapes for the absorptivity with up to a factor of 2 to the reference case of nearly spherical shaped Droxtals. The respective cirrus radiative forcing differs up to a factor of 4 with a higher cooling effect for Droxtals. A similar effect is due to an additional low-level water cloud, as observed during the measurement flights, with a noticeable difference in the reflectivity of the above lying cirrus of up to a factor of 2. The radiative forcing of the cirrus layer may switch sign and shows positive values in the near infrared wavelength range with a resulting difference of up to a factor of 4. It was found that if a low-level cloud is not considered the solar cooling of the cirrus is strongly overestimated.

The application of measured in situ microphysical properties as input of radiative transfer simulations did not accurately reproduce the measured cirrus optical layer properties. This is partly due to a variety of possible shapes and mixtures of shapes,

ACPD
15, 19045–19077, 2015

and influenced by a changing albedo. Further adjustment of the simulations can be used to optimize the agreement and derive more information on the particle properties. The effect of the low-level water cloud has to be further investigated by varying the property of the cirrus, such as shape, size, and height of the cloud base and top, and the property of the low cloud, such as optical and geometrical thickness, too. As the interaction of the cirrus with terrestrial radiation is the important factor for affecting the earth's energy budget, radiative transfer calculations in the terrestrial wavelength range have to be investigated.

Acknowledgements. This study was supported by the Deutsche Forschungsgemeinschaft through Project "WE 1900/19–1, BO 1829/7–1". Additional funding on a similar level for the aircraft certification of AIRTOSS and for conducting the campaign was provided by internal sources of the Particle Chemistry Department at the Max Planck Institute for Chemistry. We thank the pilots and crew of the Gesellschaft für Flugzieldarstellung (GFD) and enviscope GmbH for preparation and execution of the test and research flights, and the colleagues from Forschungszentrum Jülich and University of Warsaw for their support.

References

Baum, B. A., Yang, P., Heymsfield, A. J., Platnick, S., King, M. D., Hu, Y. X., and Bedka, S. T.: Bulk scattering properties for the remote sensing of ice clouds. Part II: Narrowband models, J. Appl. Meteorol., 44, 1896–1911, 2005. 19057, 19058, 19059

Baum, B. A., Yang, P., Hu, Y. X., and Feng, Q. A.: The impact of ice particle roughness on the scattering phase matrix RID B-7670-2011 RID B-4590-2011, J. Quant. Spectrosc. Ra., 111, 2534–2549, doi:10.1016/j.jqsrt.2010.07.008, 2010. 19057

Bierwirth, E., Wendisch, M., Ehrlich, A., Heese, B., Tesche, M., Althausen, D., Schladitz, A., Müller, D., Otto, S., Trautmann, T., Dinter, T., von Hoyningen-Huene, W., and Kahn, R.: Spectral surface albedo over Morocco and its impact on the radiative forcing of Saharan dust, Tellus B, 61, 252–269, 2009. 19049

Eichler, H., Ehrlich, A., Wendisch, M., Mioche, G., Gayet, J.-F., Wirth, M., Emde, C., and Minikin, A.: Influence of ice crystal shape on retrieval of cirrus optical thickness and effec-

ACPD
15, 19045–19077, 2015

tive radius: a case study, J. Geophys. Res., 114, D19203, doi:10.1029/2009JD012215, 2009. 19047
Field, P. R., Wood, R., Brown, P. R. A., Kaye, P. H., Hirst, E., Greenaway, R., and Smith, J. A.: Ice particle interarrival times measured with a fast FSSP, J. Atmos. Ocean. Tech., 20, 249–261, 2003. 19049
Field, P. R., Heymsfield, A., and Bansemer, A.: Shattering and particle interarrival times measured by optical array probes in ice clouds, J. Atmos. Ocean. Tech., 23, 1357–1370, 2006. 19049
Francis, P., Hignett, P., and Macke, A.: The retrieval of cirrus cloud properties from aircraft multi-spectral reflectance measurements during EUCREX '93, Q. J. Roy. Meteor. Soc., 124, 1273–1291, 1998. 19047
Frey, W., Eichler, H., de Reus, M., Maser, R., Wendisch, M., and Borrmann, S.: A new airborne tandem platform for collocated measurements of microphysical cloud and radiation properties, Atmos. Meas. Tech., 2, 147–158, doi:10.5194/amt-2-147-2009, 2009. 19048, 19050
Gayet, J. F., Auriol, F., Minikin, A., Strom, J., Seifert, M., Krejci, R., Petzold, A., Febvre, G., and Schumann, U.: Quantitative measurement of the microphysical and optical properties of cirrus clouds with four different in situ probes: evidence of small ice crystals, Geophys. Res. Lett., 29, 83-1–83-4 doi:10.1029/2001GL014342, 2002. 19049
Henrich, F., Siebert, H., Jäkel, E., Shaw, R. A., and Wendisch, M.: Collocated measurements of boundary-layer cloud microphysical and radiative properties and comparison with satellite retrievals, J. Geophys. Res., 115, D24214, doi:10.1029/2010JD013930, 2010. 19048
IPCC: Climate Change 2013: The Physical Science Basis, Cambridge University Press, UK and New York, NY, USA, 2013. 19046
Keil, A. and Haywood, J. M.: Solar radiative forcing by biomass burning aerosol particles during SAFARI 2000: a case study based on measured aerosol and cloud properties, J. Geophys. Res., 108, 8467, doi:10.1029/2002JD002315, 2003. 19060
Klingebiel, M., de Lozar, A., Molleker, S., Weigel, R., Roth, A., Schmidt, L., Meyer, J., Ehrlich, A., Neuber, R., Wendisch, M., and Borrmann, S.: Arctic low-level boundary layer clouds: in situ measurements and simulations of mono- and bimodal supercooled droplet size distributions at the top layer of liquid phase clouds, Atmos. Chem. Phys., 15, 617–631, doi:10.5194/acp-15-617-2015, 2015. 19049

ACPD
15, 19045–19077, 2015

Korolev, A. V., Emery, E. F., Strapp, J. W., Cober, S. G., and Isaac, G. A.: Quantification of the effects of shattering on airborne ice particle measurements, J. Atmos. Ocean. Tech., 30, 2527–2553, 2013. 19049

Liou, K.-N.: Influence of cirrus clouds on weather and climate processes: a global perspective, Mon. Weather Rev., 114, 1167–1199, 1986. 19047

Lynch, K., Sassen, K., Starr, D., Stephens, G., Heymsfield, A., Liou, K.-N., Minnis, P., and Platt, C.: Cirrus, Oxford University Press, New York, 2002. 19046

Mayer, B. and Kylling, A.: Technical note: The libRadtran software package for radiative transfer calculations – description and examples of use, Atmos. Chem. Phys., 5, 1855–1877, doi:10.5194/acp-5-1855-2005, 2005. 19054, 19056

McFarquhar, G. M., Um, J., Freer, M., Baumgardner, D., Kok, G. L., and Mace, G.: Importance of small ice crystals to cirrus properties: observations from the Tropical Warm Pool International Cloud Experiment (TWP-ICE), Geophys. Res. Lett., 34, L13803, doi:10.1029/2007GL029865, 2007. 19050

Müller, S., Hoor, P., Berkes, F., Bozem, H., Klingebiel, M., Reutter, P., Smit, H. G. J., Wendisch, M., Spichtinger, P., and Borrman, S.: In-situ detection of stratosphere-troposphere-exchange of cirrus particles in the mid-latitudes, Geophys. Res. Lett., 42, 949–955, doi:10.1002/2014GL062556, 2015. 19052

Pilewskie, P. and Valero, F. P. J.: Radiative effects of the smoke clouds from the Kuwait oil fires, J. Geophys. Res., 97, 14541–14544, 1992. 19047

Schlimme, I., Macke, A., and Reichardt, J.: The impact of ice crystal shapes, size distributions, and spatial structures of cirrus clouds on solar radiative fluxes, J. Atmos. Sci., 62, 2274–2283, 2005. 19047

Stamnes, K., Tsay, S.-C., Wiscombe, W., and Laszlo, I.: DISORT, a General-Purpose Fortran Program for Discrete-Ordinate-Method Radiative Transfer in Scattering and Emitting Layered Media: Documentation of Methodology, Tech. rep, Dept. of Physics and Engineering Physics, Stevens Institute of Technology, Hoboken, NJ 07030, 2000. 19056

Wendisch, M. and Brenguier, J.-L.: Airborne Measurements for Environmental Research – Methods and Instruments, Wiley–VCH Verlag GmbH and Co. KGaA, Weinheim, Germany, ISBN: 978-3-527-40996-9, 2013. 19049

Wendisch, M., Müller, D., Schell, D., and Heintzenberg, J.: An airborne spectral albedometer with active horizontal stabilization, J. Atmos. Ocean. Tech., 18, 1856–1866, 2001. 19049

ACPD
15, 19045–19077, 2015

Wendisch, M., Pilewskie, P., Pommier, J., Howard, S., Yang, P., Heymsfield, A. J., Schmitt, C. G., Baumgardner, D., and Mayer, B.: Impact of cirrus crystal shape on solar spectral irradiance: a case study for subtropical cirrus, J. Geophys. Res., 110, D03202, doi:10.1029/2004JD005294, 2005. 19047, 19057

Wendisch, M., Yang, P., and Pilewskie, P.: Effects of ice crystal habit on thermal infrared radiative properties and forcing of cirrus, J. Geophys. Res., 112, D03202, doi:10.1029/2006JD007899, 2007. 19047

Werner, F., Siebert, H., Pilewskie, P., Schmeissner, T., Shaw, R. A., and Wendisch, M.: New airborne retrieval approach for trade wind cumulus properties under overlying cirrus, J. Geophys. Res., 118, 3634–3649, doi:10.1002/jgrd.50334, 2013. 19048

Werner, F., Ditas, F., Siebert, H., Simmel, M., Wehner, B., Pilewskie, P., Schmeissner, T., Shaw, R. A., Hartmann, S., Wex, H., Roberts, G. C., and Wendisch, M.: Twomey effect observed from collocated microphysical and remote sensing measurements over shallow cumulus, J. Geophys. Res., 119, 1534–1545, doi:10.1002/2013JD020131, 2014. 19048

Wylie, D., Menzel, W., Woolf, H., and Strabala, K.: Four years of global cirrus cloud statistics using HIRS, J. Climate, 7, 1972–1986, 1994. 19047

Yang, P., Wei, H. L., Huang, H. L., Baum, B. A., Hu, Y. X., Kattawar, G. W., Mishchenko, M. I., and Fu, Q.: Scattering and absorption property database for nonspherical ice particles in the near- through far-infrared spectral region, Appl. Optics, 44, 5512–5523, 2005. 19056

Yang, P., Bi, L., Baum, B. A., Liou, K. N., Kattawar, G. W., Mishchenko, M. I., and Cole, B.: Spectrall consistent scatterin, absorption, and polarization properties of atmospheric ice crystals at wavelengths from 0.2 to 100 µm, J. Atmos. Sci., 70, 330–347, 2013. 19057

Zhang, Y., Macke, A., and Albers, F.: Effect of crystal size spectrum and crystal shape on stratiform cirrus radiative forcing, Atmos. Res., 52, 59–75, 1999. 19047

ACPD
15, 19045–19077, 2015

Figure 1. Photo from the Learjet 35A with towed AIRTOSS. The picture was taken during a test flight from a second aircraft.

ACPD
15, 19045–19077, 2015

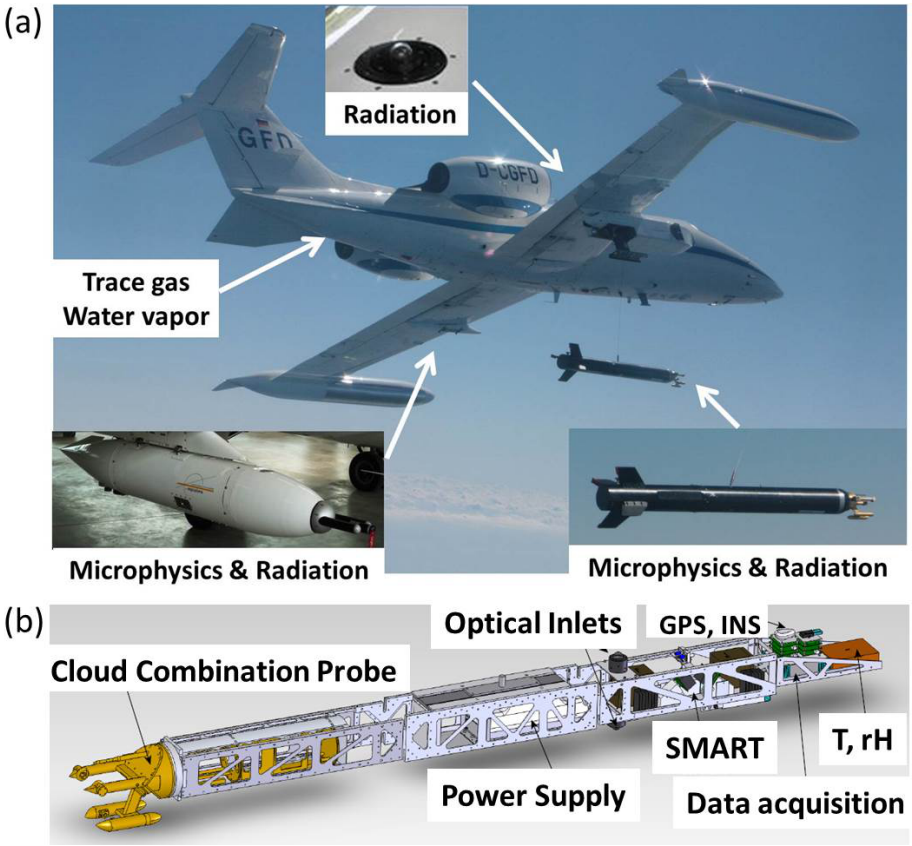

Figure 2. (a) Assembly of the research aircraft Learjet 35A, the towed AIRTOSS, and the wing pod containing instruments measuring radiation, microphysical parameter, water vapor, and trace gases. **(b)** Sketch of the AIRTOSS setup.

ACPD
15, 19045–19077, 2015

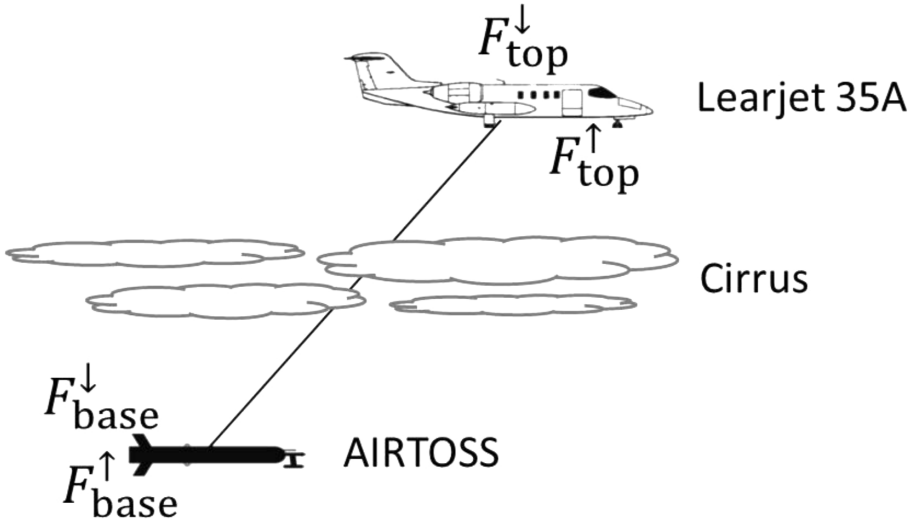

Figure 3. Schematic sketch of measurement setup to measure collocated upward ($F^{\uparrow}$) and downward ($F^{\downarrow}$) irradiance at two altitudes (base, top).

ACPD
15, 19045–19077, 2015

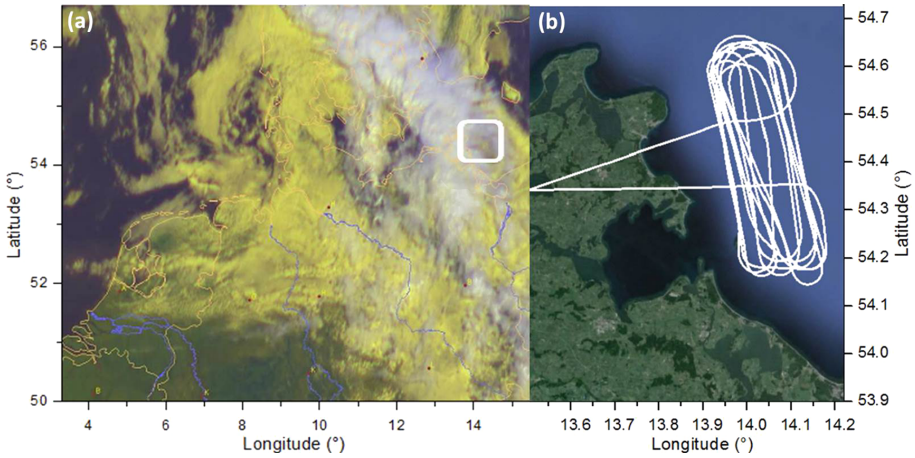

Figure 4. (a) Composite satellite image of the cloud situation on 4 September 2013 at 10:00 UTC showing cirrus (white) above yellow colored lower water clouds (Deutscher Wetterdienst/EUMETSAT). In **(b)** the flight track of the measuring flight in the restricted area (white box in **a**) above the Baltic Sea near the island of Rügen, North Germany, is shown.

ACPD
15, 19045–19077, 2015

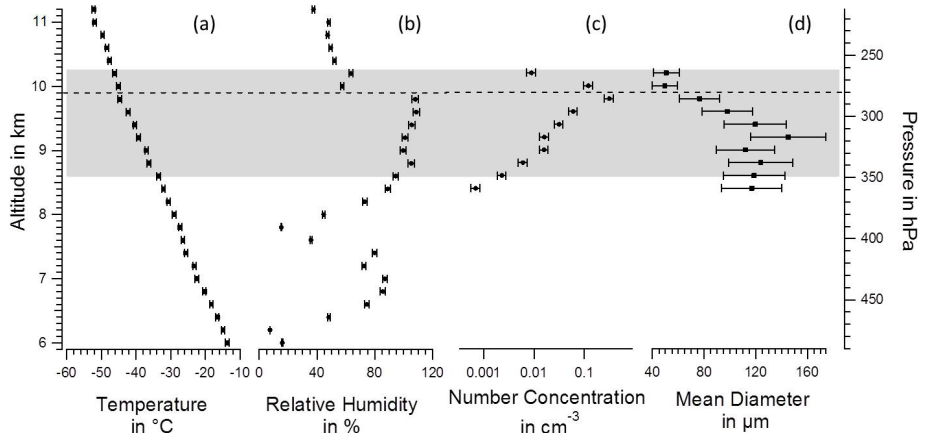

Figure 5. Vertical profiles of **(a)** temperature, **(b)** relative humidity, measured on the Learjet 35A, **(c)** number concentration, and **(d)** mean diameter, derived by CCP on AIRTOSS, from the flight of 4 September 2013. The bars show the corresponding measurement uncertainties. The gray area shows the cirrus layer. The horizontal dashed line indicates the altitude above which stratospheric air was encountered.

ACPD
15, 19045–19077, 2015

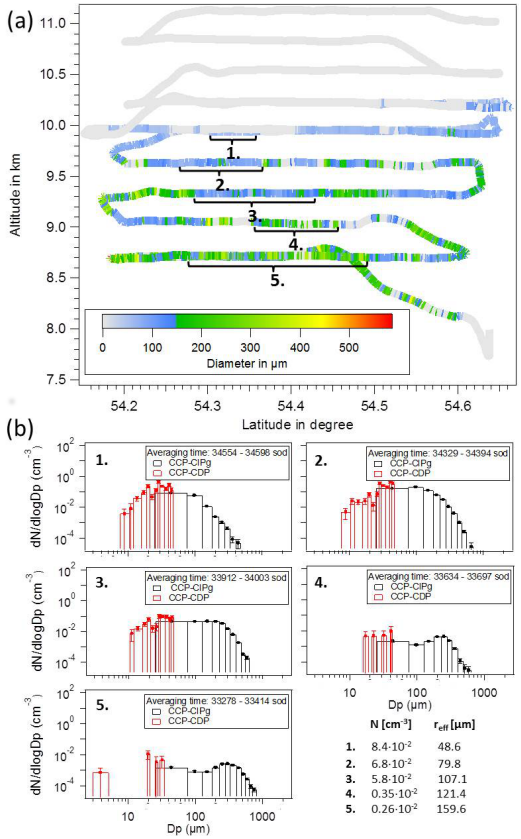

Figure 6. (a) Vertical profile of mean diameter, represented in the flight track from the flight of 4 September 2013. **(b)** shows number size distributions in terms of equivalent cloud particle diameter D_p corresponding to marked segments in **(a)**. The error bars reflect counting statistics and the uncertainty of the optical volume. The table shows respective number concentrations N and r_{eff}.

ACPD
15, 19045–19077, 2015

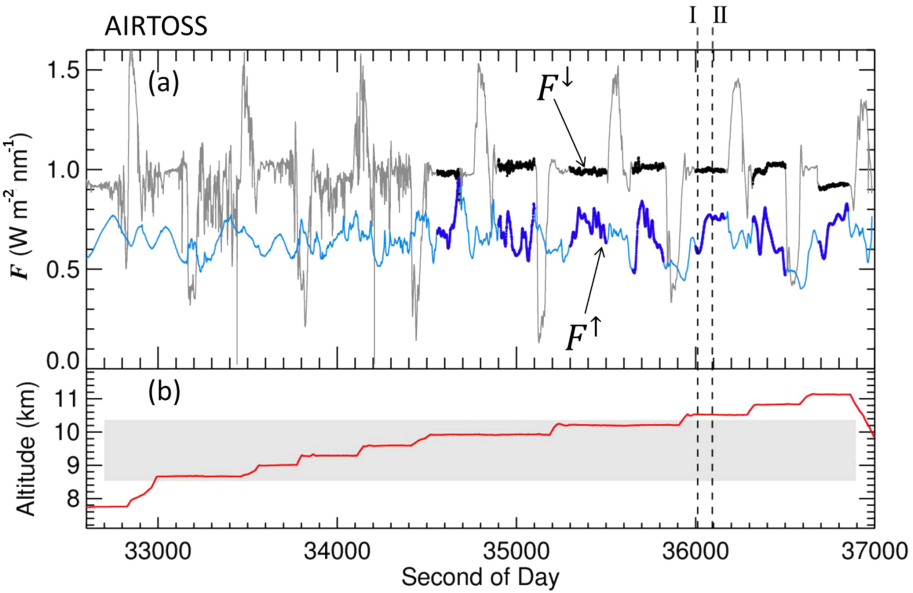

Figure 7. (a) Time series of downward (gray) and upward (light blue) irradiance F (W m^{-2} nm^{-1}) measured on AIRTOSS at one wavelength (550 nm) from the flight of 4 September 2013. The thickened line periods mark the measuring points at straight flight legs. The red line in **(b)** shows the altitude of AIRTOSS with the cloud layer, indicated by a gray area. The vertical dashed lines mark different conditions below the cirrus: (I) cloudless and (II) a low cloud is present.

ACPD
15, 19045–19077, 2015

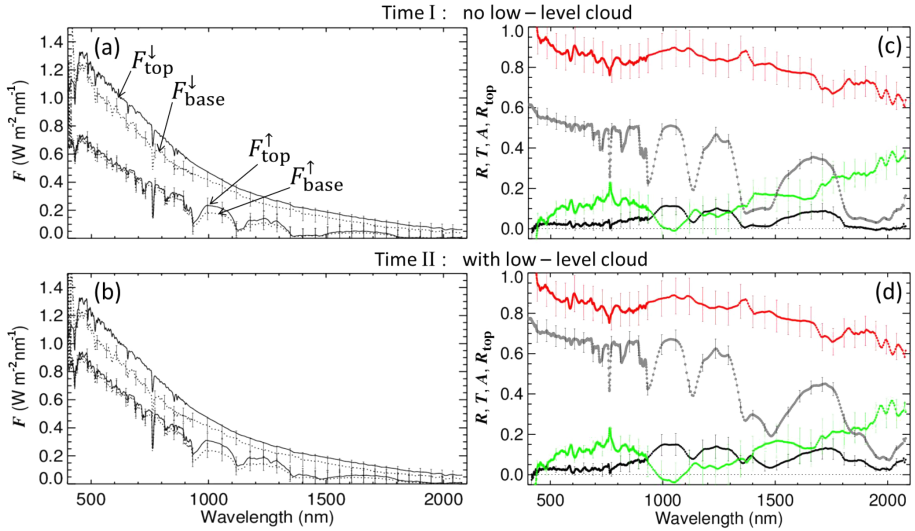

Figure 8. (a, b) show measured spectral downward and upward irradiance F from the aircraft above the cloud layer (solid lines) and AIRTOSS below the cloud layer (dotted lines) at two times I and II, indicated by the vertical dashed lines in Fig. 7. $F^{\downarrow}_{top}$ is simulated. **(c, d)** show spectral reflectivity (black), transmissivity (red), absorptivity (green), and cloud top albedo (gray) according to irradiance in **(a, b)**. The vertical bars indicate the systematic errors due to measurement uncertainties.

ACPD
15, 19045–19077, 2015

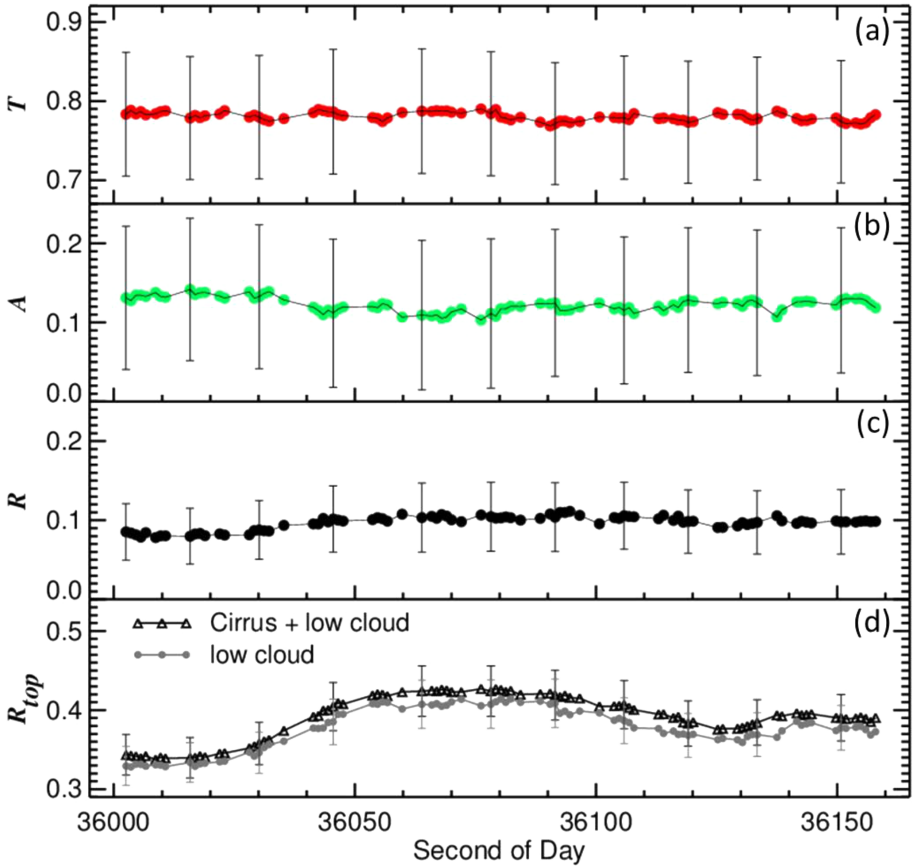

Figure 9. Shown are time series of **(a)** transmissivity, **(b)** absorptivity, and **(c)** reflectivity (at 1640 nm) for the cirrus layer between 10.6 and 10.8 km altitude on 4 September 2013. The associated cloud top albedo above (Cirrus + low cloud) and below (low cloud) this cirrus layer is plotted in **(d)**. The vertical bars represent the errors due to measurement uncertainties.

ACPD
15, 19045–19077, 2015

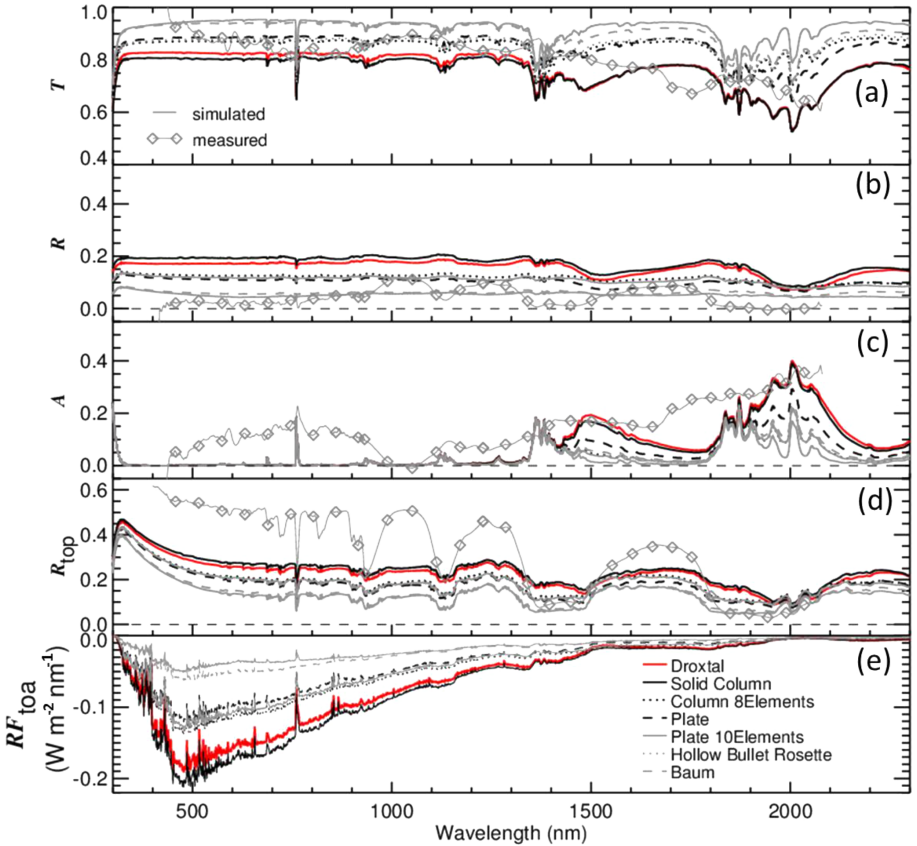

Figure 10. The lines show spectral **(a)** transmissivity, **(b)** reflectivity, **(c)** absorptivity, and **(d)** cloud top albedo of a cirrus layer between 8.6 and 10.3 km altitude. The simulations are based on a measured number size distribution from 4 September 2013 assuming different ice particle shapes. **(e)** are the radiative forcings at TOA, respectively. Inserted is the measurement case I (gray diamonds).

ACPD
15, 19045–19077, 2015

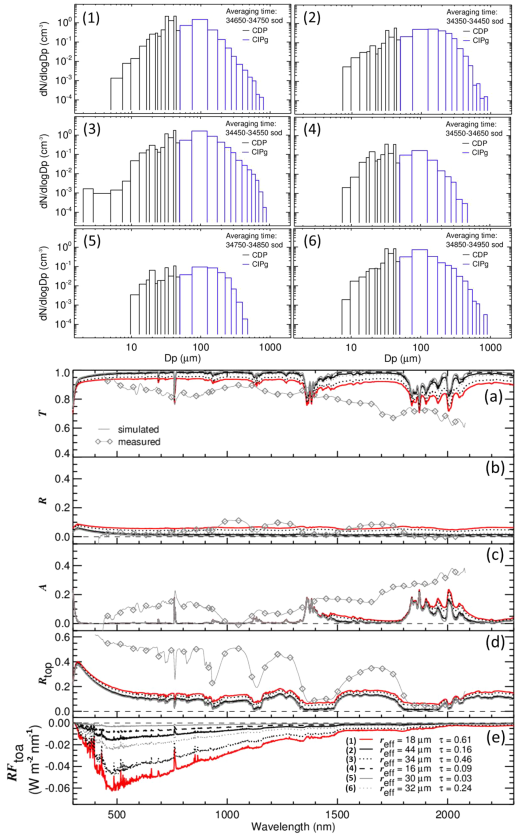

Figure 11. Same as Fig. 10 for different included number size distributions, shown in the upper panel (1)–(6). Inserted is the measurement case I (gray diamonds).

ACPD
15, 19045–19077, 2015

Spectral optical layer properties of cirrus from collocated airborne measurements

F. Finger et al.

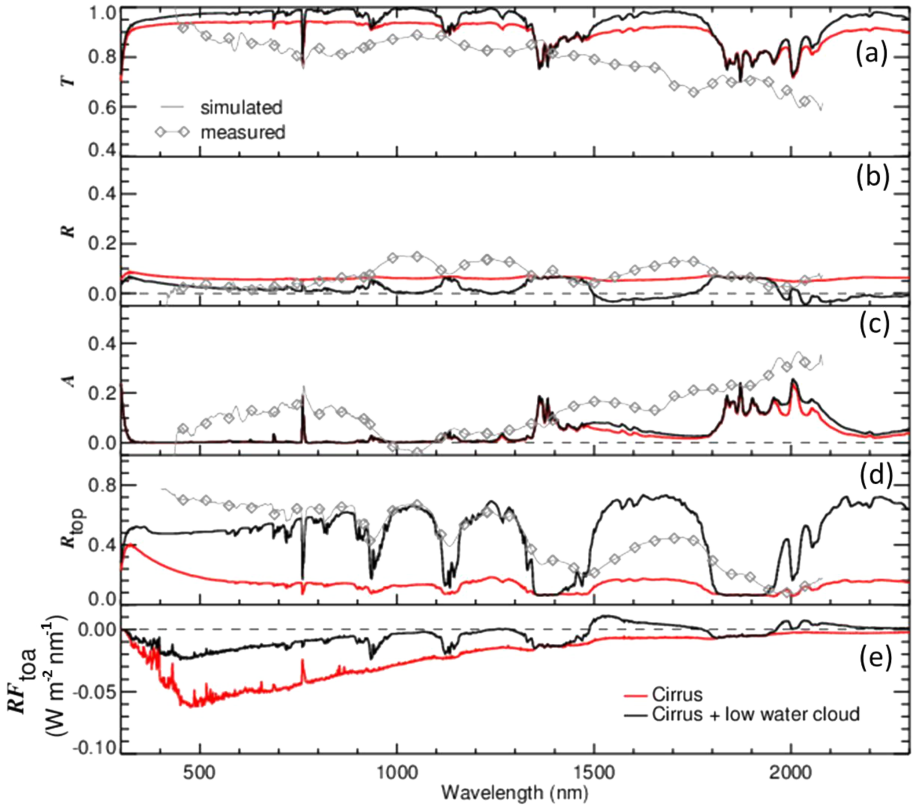

Figure 12. Same as Fig. 10 with an additional low water cloud between 1.5 and 1.75 km altitude with τ = 45 included. Inserted is the measurement case II (gray diamonds).

ACPD
15, 19045–19077, 2015

Spectral optical layer properties of cirrus from collocated airborne measurements

F. Finger et al.